Multi-Coset Sparse Imaging Arrays

James D. Krieger, Yuval Kochman, *Member, IEEE*, and Gregory W. Wornell, *Fellow, IEEE*

***Abstract*—We develop an efficient structured sparse antenna array architecture for coherent imaging of sparse but otherwise unknown scenes. In this architecture, the array elements are configured in a periodic nonuniform pattern that can be viewed as the superposition of multiple sparse uniform subarrays. For such structure, we develop an efficient pattern design procedure using co-array analysis, and we describe robust and efficient algorithms implementing the required associated array processing, which comprise scene support recovery, followed by image reconstruction. In addition, we develop a practical method for detecting reconstruction failures when the scene density exceeds the level for which the array was designed, so that false images are not produced. As a demonstration of its viability, the architecture is used to reconstruct a simulated natural scene.**

***Index Terms*—Compressed sensing, millimeter-wave imaging, MUSIC algorithm, phased-array antennas, sparse arrays.**

I. INTRODUCTION

RECENT advances in millimeter-wave technology, including the advent of terahertz CMOS circuits, have the potential to enable, for the first time, a host of low-cost imaging and "personal radar" applications. Indeed, at these higher frequencies, typical resolution requirements can be met with comparatively compact arrays, which are especially attractive for applications requiring some degree of mobility. Moreover, such arrays can be implemented with inexpensive integrated circuit and antenna technologies, and digital implementations.

However, with such technology come significant new challenges, an important example of which is the large number of array elements typically required to construct a phased array in such applications. As an illustration, in a vehicle collision avoidance system, obtaining sufficient resolution might require an aperture of roughly 2 m. But in this case a traditional phased array operating at 100 GHz with half-wavelength element spacing would require roughly 1000 antennas, which is daunting to implement. Indeed, such arrays are costly and complex to design and calibrate, and, moreover, since the system processing requirements scale in proportion to the number of elements, the needed computational bandwidth quickly becomes impractically large.

As a result, there is renewed interest in developing sparse antenna array architectures. Sparse arrays, characterized by average inter-element spacings greater than one half of the operating wavelength, have been of interest throughout much of the history of phased arrays, garnering a great deal of attention in the early 1960's; see, e.g., [1] and references therein.

The design of general-purpose sparse arrays has typically entailed making basic performance tradeoffs. A well-known example is the use of "density tapering," which uses a gradually increasing spacing profile as one moves from the center toward the edges of the aperture. These arrays are representative of a class of "thinned" arrays that stretch the aperture associated with a given number of elements to achieve a desired resolution by narrowing the width of the main lobe without introducing additional grating lobes. However, this is obtained at the cost of a significant increase in the side lobe level. For certain applications in which resolution is the key performance metric, these provide a useful design solution. However, in the context of imaging arrays this introduces an unacceptable noise floor.

Another class of sparse arrays, referred to as *limited scan* arrays, accommodate sparseness by constraining the field-of-view of the array to a commensurately narrow range of angles [2]. This may be accomplished through the use of lens or reflector systems designed to increase the directive properties of the array elements such that grating lobes are suppressed outside of the angular region of interest. However, such arrays must be rotated physically in order to provide wide angle coverage, requiring relatively static environments as well as increased mechanical complexity.

The need for mechanical steering of limited scan arrays can be avoided without requiring additional digital processing through the use of overlapped subarray antennas [3], in which the array elements are connected to multiple subarrays. Each subarray acts as an analog beamformer, suppressing signals outside of the desired sector. By connecting digital receivers to the subarrays, full coverage throughout the sector is accomplished in the digital domain. With this architecture, the number of required receivers decreases linearly with the size of the sector. In turn, full coverage can be achieved through a combination of element-level phase shifters and subarray-level digital receivers.

In this paper, we take a different approach, whereby rather than constraining the functionality or performance of the array, we exploit structure in the scene being imaged. In particular, we seek to exploit sparsity in the scene to allow the number of antenna elements to be reduced. Specifically, when the scene being imaged is sparse in an appropriate sense—even without

Manuscript received December 01, 2012; manuscript revised June 26, 2013; accepted September 22, 2013. Date of publication January 13, 2014; date of current version April 03, 2014. This work was supported in part by the National Science Foundation under Grant No.CCF-1017772, in part by the Semiconductor Research Corporation through the Focus Center Research Program's Center for Circuits System Solutions (C2S2), and in part by the United States Air Force under Contract No. FA8721-05-C-0002. Opinions, interpretations, conclusions and recommendations are those of the authors and are not necessarily endorsed by the United States Government.

J. D. Krieger and G. W. Wornell are with the Department of Electrical Engineering and Computer Science, Massachusetts Institute of Technology, Cambridge, MA 02139 USA (e-mail: jameskrieger@mit.edu; gww@mit.edu).

Y. Kochman is with the School of Computer Science and Engineering, Hebrew University of Jerusalem, Jerusalem, Israel (e-mail: yuvalko@cs.huji.ac.il).

Digital Object Identifier 10.1109/TAP.2014.2299819

knowing *where* it is sparse—it is possible to proportionally reduce the number of elements in an imaging array. Moreover, such sparseness is quite common in typical applications.[1]

This approach also has a rich history. Consider, for example, the classical problem of direction-finding with multiple sources, for which the MUSIC algorithm [4], among others, was developed. In this case, it is possible to achieve high resolution with relatively few antenna elements because of the sparse nature of the scene. Indeed, the number of elements required is typically on the order of the number of sources. Hence, the presence of structure in the environment allows the number of elements to be reduced.

For arrays containing just a few elements, the array design and image reconstruction can often be fairly straightforward and exploit classical techniques. However, for arrays of even a few dozen elements, the implementation of such direct approaches quickly becomes computationally impractical. As a result, there is a need to impose useful structure on the array to enable efficient design and processing.

There has been growing recent interest in nonuniform arrays with structure, and how such structure can be exploited by efficient array processing to support forms of sparse sensing; see, e.g., [5]–[11]. Ultimately, these developments leverage perspectives and techniques from the field of compressive sensing (CS) [12], [13].

In our development, we focus on particular structured sparse antenna designs that are comparatively easy to design and for which efficient array processing algorithms can be developed to perform the image reconstruction. Specifically, we focus on "multi-coset" arrays, defined as a collection of interleaved sparse uniform subarrays such that the elements are laid out in a periodic nonuniform pattern over the aperture.

This special structure has important computational implications. In particular, as will become apparent, the complexity of the associated array processing for such arrays is effectively governed by the number of elements in a period of the array, not by the total number of elements—i.e., the complexity does not significantly depend on the number of periods of the pattern in the array. As a result, the practicality of our architecture is not limited to arrays consisting of only very small numbers of elements, as has historically often been the case with less judiciously structured nonuniform arrays.

This array architecture, introduced in [5] for our application,[2] follows from exploiting the close mathematical relationship between the problem of imaging from a discrete array, and that of reconstructing a bandlimited time-domain waveform from samples. Indeed, our architecture is the counterpart of multi-coset sampling [14]. And while [5] focuses on making the mathematical connection between these domains, the present paper represents a more complete development of the design and analysis of multi-coset sparse imaging arrays in their own right.

The paper is organized as follows. Section II defines the array structure and scene model of interest. Section III develops the basic multi-coset imaging principles and concepts for the paper. Section IV analyzes the effects of noise in multi-coset imaging, and develops suitable robust multi-coset array processing techniques. Section V then develops a co-array framework for the design of multi-coset arrays, and uses this framework to identify a diverse family of effective patterns. Section VI develops a methodology for reliably detecting reconstruction failures when the scene density exceeds the level for which an array is designed. As an illustration of potential, Section VII develops and demonstrates the use of multi-coset imaging in a realistic scenario. Finally, Section VIII contains some concluding remarks.

II. ARRAY STRUCTURE AND SCENE MODEL

Throughout this paper, we focus on linear arrays of elements located on some subset of collinear lattice points with uniform spacing $d = \lambda/2$, where λ is the operating wavelength of the array. We assume ideal isotropic elements and limit our attention to the half-plane such that the directional characteristics of the array are completely specified by the angle θ, measured from the broadside direction of the array.

A standard linear array refers to any array having uniform element spacing of $\lambda/2$. Substituting $\psi = \sin\theta/2$, we see the array response and far-field pattern for a standard array with $N \to \infty$ elements forming the usual Fourier transform pair

$$x[n] = \int_0^1 X(\psi) e^{j2\pi\psi n}\, \mathrm{d}\psi, \qquad n \in \mathbb{Z} \tag{1}$$

$$X(\psi) = \sum_{n=0}^{N-1} x[n] e^{-j2\pi\psi n}, \qquad \psi \in [0,1). \tag{2}$$

From the view of array imaging, (1) describes $x[n]$ as the response at element n to a scene consisting of complex valued objects $X(\psi)$. Standard reconstruction (delay-and-sum beamforming) of the scene in a given direction ψ is carried out using (2).

The multi-coset arrays of interest in this work are subsets of a standard linear array. Specifically, for an integer parameter L, we can partition the N elements of any standard array into L cosets. Each coset is a uniform linear subarray with inter-element spacing L times greater than the nominal spacing. We index the cosets by the position of their first element relative to the first element of the full array. A multi-coset array comprises a subset of these cosets. In particular, for $P \leq L$, a (P, L) multi-coset array is an array formed by including P of these cosets. The selected cosets are denoted via

$$\mathcal{P} = \{p_0, p_1, \dots, p_{P-1}\},$$

with $0 \leq p_0 < p_1 < \cdots < p_{P-1} \leq L-1$, and referred to as the *coset pattern* of the array. Note that the resulting array has a recurrent uniform pattern with period L, and thus we refer to L as the *coset period*. As further notation, there are $M = N/L$ such periods in the array. As an example, Fig. 1 depicts the layout of a $(4, 7)$ multi-coset array with coset pattern $\mathcal{P} = \{0, 1, 2, 4\}$ superimposed on the lattice of the associated standard linear array from which it was derived.

---

[1] Note that in a typical scene while there are objects at some range in any particular direction, when we use enough bandwidth to sufficiently resolve range as well, we find significant sparseness in the range-azimuth plane.

[2] See also [6] for related applications.

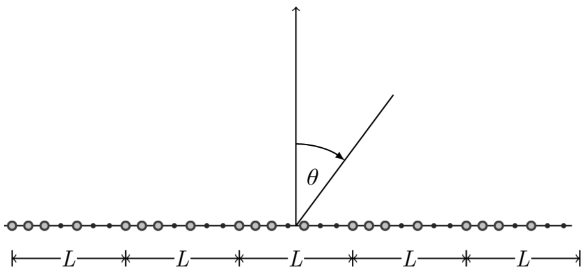

Fig. 1. $(P, L) = (4, 7)$ multi-coset array with coset pattern $\mathcal{P} = \{0, 1, 2, 4\}$ and $M = 5$ coset periods.

The response for coset p is defined via

$$x^{(p)}[n] \triangleq x[n] \sum_{m=0}^{M-1} \delta[n - (mL + p)], \;\; p \in \{0, 1, \dots, L-1\} \tag{3}$$

for $n = 0, 1, \dots, N-1$, where

$$\delta[k] \triangleq \begin{cases} 1 & k = 0 \\ 0 & \text{otherwise.} \end{cases}$$

The corresponding coset image in the angular domain is given by the Fourier transform of the coset response, i.e.,

$$X^{(p)}(\psi) = \sum_n x^{(p)}[n]\, e^{-j2\pi\psi n}, \quad \psi \in [0, 1). \tag{4}$$

The individual coset images in (4) contain L uniformly shifted copies of the original scene due to the aliasing effect caused by the increased element spacing Ld. As a result, the coset image appears as L sectors, each containing grating lobes from the other $L-1$ sectors in addition to the correct response. Combining (1), (3), and (4), the coset image in the first sector can be written as a linear combination of the grating lobes of the original scene

$$X^{(p)}(\psi) = \frac{1}{L} \sum_{q=0}^{L-1} X\left(\psi + \frac{q}{L}\right) e^{j2\pi pq/L}, \quad \psi \in \Big[0, 1/L\Big). \tag{5}$$

The goal in multi-coset image reconstruction is to extract the entire correct image from the images of multiple cosets in a single sector. While this is in general not possible, it is possible in scenarios where there are imaging targets in only a subset of the L sectors in the original scene, which we refer to as *sector sparsity*. More specifically, for any pair of integers $Q \leq L$, we say that a scene is (Q, L)-sparse if $X(\psi) = 0$ for all $\psi \notin \mathcal{S}$, where

$$\mathcal{S} = \bigcup_{k=0}^{Q-1} \left[\frac{q_k}{L}, \frac{q_k + 1}{L}\right) \tag{6}$$

where the q_k are integer-valued elements satisfying $0 \leq q_0 < q_1 < \cdots < q_{Q-1} \leq L - 1$. The set

$$\mathcal{Q} = \{q_0, q_1, \dots, q_{Q-1}\},$$

is referred to as the *(sector) support* of the scene. An example of a $(3, 7)$-sparse scene is shown in Fig. 2.

The array structure and scene model above is the spatial counterpart of temporal framework originally introduced [14], which developed the use of multi-coset sampling for signals with sparse spectral support.

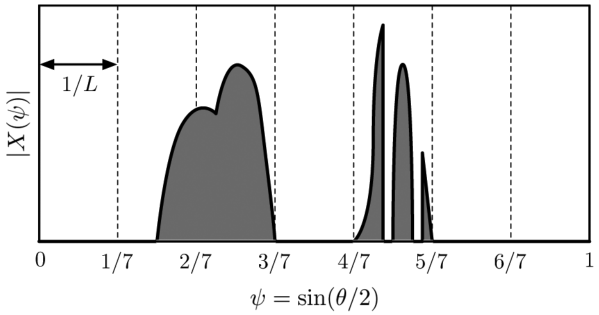

Fig. 2. $(Q, L) = (3, 7)$-sparse scene with support $\mathcal{Q} = \{1, 2, 4\}$.

In the sequel, we describe when and how image reconstruction is possible with multi-coset arrays for sector sparse scenes.

III. MULTI-COSET IMAGING PRINCIPLES

In this section, we summarize the basic principles underlying multi-coset imaging of sector sparse scenes, and introduce our notation for the remainder of the paper. Subsequent sections will then build on this foundation, incorporating the effects of noise and developing robust system design.

In our architecture, imaging proceeds in two phases: the first phase recovers the sector support of the scene, while the second phase reconstructs the signal values (targets) in the active sectors identified in the first phase.

A. Reconstruction With Known Support

We begin by developing the properties of scene reconstruction when the sector support is known, corresponding to the second phase of the imaging process. This reconstruction can be expressed as the solution to a set of (possibly) redundant linear equations.

To see this, we first define, for $p \in \{0, 1, \dots, L-1\}$,

$$Y_p(\psi) \triangleq X^{(p)}(\psi)\, H(\psi), \tag{7}$$

$$X_q(\psi) \triangleq X\left(\psi + \frac{q}{L}\right) H(\psi), \tag{8}$$

with

$$H(\psi) \triangleq \begin{cases} 1 & \psi \in \Big[0, 1/L\Big) \\ 0 & \text{otherwise,} \end{cases}$$

from which we can express (5) in the form

$$Y_p(\psi) = \sum_{q=0}^{L-1} F_{pq} X_q(\psi) \quad \text{with} \quad F_{pq} \triangleq \frac{1}{L} e^{j2\pi pq/L} \tag{9}$$

or, equivalently, $\mathbf{Y}(\psi) = \mathbf{F}\mathbf{X}(\psi)$, where $[\mathbf{Y}(\psi)]_p = Y_p(\psi)$, $[\mathbf{X}(\psi)]_q = X_q(\psi)$, and $[\mathbf{F}]_{pq} = F_{pq}$.

From (9) we see that the $\{X_q(\psi)\}$ may be directly recovered from the complete set of coset responses $\{Y_p(\psi)\}$. And once these quantities are recovered, image reconstruction is completed via

$$X(\psi) = \sum_{q=0}^{L-1} X_q\left(\psi - \frac{q}{L}\right). \tag{10}$$

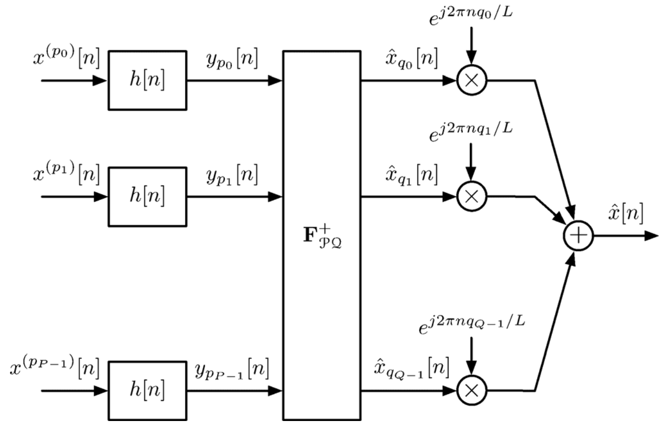

Fig. 3. Multi-coset reconstruction processing chain.

In the case of a (P, L) sparse multi-coset array, we must consider instead the length-P vector $\mathbf{Y}_{\mathcal{P}}(\psi)$, composed of the entries of $\mathbf{Y}(\psi)$ indexed by the coset pattern $\mathcal{P}$. Similarly, we define the $P \times L$ matrix $\mathbf{F}_{\mathcal{P}}$ containing the P rows of $\mathbf{F}$ indexed by $\mathcal{P}$. This results in the relation

$$\mathbf{Y}_{\mathcal{P}}(\psi) = \mathbf{F}_{\mathcal{P}}\mathbf{X}(\psi). \tag{11}$$

In this form, we now have an undetermined system, having an infinite number of possible solutions.

For a (Q, L)-sparse scene with support $\mathcal{Q}$, the elements of $\mathbf{X}(\psi)$ not indexed by this support are zero-valued, and thus do not contribute to the coset responses. Hence, we may define the $P \times Q$ *measurement matrix* $\mathbf{F}_{\mathcal{PQ}}$, composed of the columns of $\mathbf{F}_{\mathcal{P}}$ indexed by $\mathcal{Q}$, and the length-Q vector $\mathbf{X}_{\mathcal{Q}}(\psi)$ containing the nonzero entries of $\mathbf{X}(\psi)$. The updated relation becomes

$$\mathbf{Y}_{\mathcal{P}}(\psi) = \mathbf{F}_{\mathcal{PQ}}\mathbf{X}_{\mathcal{Q}}(\psi). \tag{12}$$

If $\mathbf{F}_{\mathcal{PQ}}$ is full rank, the correct image may be reconstructed as

$$\hat{\mathbf{X}}_{\mathcal{Q}}(\psi) = \mathbf{F}^{+}_{\mathcal{PQ}}\mathbf{Y}_{\mathcal{P}}(\psi) \tag{13}$$

where $\mathbf{F}^{+}_{\mathcal{PQ}} = (\mathbf{F}^{\dagger}_{\mathcal{PQ}}\mathbf{F}_{\mathcal{PQ}})^{-1}\mathbf{F}^{\dagger}_{\mathcal{PQ}}$ is the Moore-Penrose pseudo-inverse of the matrix $\mathbf{F}_{\mathcal{PQ}}$, with † denoting the conjugate-transpose operator.

In practice, it is straightforward to ensure that the reconstruction (13) exists. In particular, the rank of $\mathbf{F}_{\mathcal{PQ}}$ depends on both $\mathcal{P}$ and $\mathcal{Q}$. A pattern $\mathcal{P}$ that ensures $\mathbf{F}_{\mathcal{PQ}}$ is full rank for any support of length Q is called a universal pattern. As shown in [14], such patterns exist whenever $P \geq Q$. For example, the so-called "bunched" pattern, in which the first P cosets are selected, i.e., $\mathcal{P}_{\mathrm{b}} = \{0, 1, \ldots, P-1\}$, is generally universal, though we will ultimately be interested in still better patterns.

1) System Implementation: The basic architecture described in this section admits a convenient implementation. In particular, the required processing is straightforward to carry out on the coset responses $x^{(p)}[n]$ directly in the array domain, and takes the form depicted in Fig. 3.

As the first step, corresponding to (7), the coset responses are passed through a linear time-invariant filter with unit-sample response $h[n]$ (whose Fourier transform is $H(\psi)$), to form the entries of the output vector sequence $\mathbf{y}_{\mathcal{P}}[n]$. From this array domain perspective, we see that the entries of $\mathbf{y}_{\mathcal{P}}[n]$ are the interpolated coset responses, generating $L-1$ values between each coset element via the interpolating filter $h[n]$.

As the second step, corresponding to expressing (12) in the following array domain form

$$\mathbf{y}_{\mathcal{P}}[n] = \mathbf{F}_{\mathcal{PQ}}\,\mathbf{x}_{\mathcal{Q}}[n] \tag{14}$$

we generate the reconstruction $\hat{\mathbf{x}}_{\mathcal{Q}}[n] = \mathbf{F}^{+}_{\mathcal{PQ}}\mathbf{y}_{\mathcal{P}}[n]$ by applying the $Q \times P$ matrix $\mathbf{F}^{+}_{\mathcal{PQ}}$ to obtain the $\hat{\mathbf{x}}_{\mathcal{Q}}[n]$.

As the final step, corresponding to the following array domain version of (10)

$$x[n] = \sum_{q=0}^{L-1} x_q[n]\, e^{j2\pi nq/L} \tag{15}$$

we have that the complete array response $\hat{x}[n]$ may be formed in the array domain by modulating and summing the Q contributions from $\hat{\mathbf{x}}_{\mathcal{Q}}[n]$.

B. Support Recovery

We next consider the first phase of imaging, corresponding to determining the active sectors in the scene, i.e., the sectors containing nonzero signal content. In this phase, Q is treated as known, and we seek to recover the sector support $\mathcal{Q}$.

Since $X_q(\psi) = 0$ for all $\psi \in [0, 1/L)$ when $q \notin \mathcal{Q}$, the recovery of $\mathcal{Q}$ via (11) can be viewed as an infinite-dimensional version of what is known in the CS literature as a *multiple measurement vector* (MMV) problem. However, it is straightforward to reduce the problem to a finite-dimensional one through a representation in terms of correlation matrices. In particular, with

$$\mathbf{R}_{\mathbf{Y}_{\mathcal{P}}} = \int_0^{1/L} \mathbf{Y}_{\mathcal{P}}(\psi)\mathbf{Y}^{\dagger}_{\mathcal{P}}(\psi)\,\mathrm{d}\psi \in \mathbb{C}^{P\times P} \tag{16}$$

denoting the coset correlation matrix, we have

$$\mathbf{R}_{\mathbf{Y}_{\mathcal{P}}} = \mathbf{F}_{\mathcal{P}}\mathbf{R}_{\mathbf{X}}\mathbf{F}^{\dagger}_{\mathcal{P}} \tag{17}$$

where each column of the scene correlation matrix

$$\mathbf{R}_{\mathbf{X}} = \int_0^{1/L} \mathbf{X}(\psi)\mathbf{X}^{\dagger}(\psi)\,\mathrm{d}\psi \in \mathbb{C}^{L\times L} \tag{18}$$

shares the sparsity structure of $\mathbf{X}(\psi)$. Namely, the rows of $\mathbf{R}_{\mathbf{X}}$ that are non-identically zero are limited to those indexed by $\mathcal{Q}$.

Since the coset correlation matrix is positive semi-definite, the eigenvalue decomposition $\mathbf{R}_{\mathbf{Y}_{\mathcal{P}}} = \mathbf{U}\boldsymbol{\Lambda}\mathbf{U}^{\dagger}$ can be used to form the size $P \times r$ matrix $\mathbf{V}$, composed of the $r = \operatorname{rank}(\mathbf{R}_{\mathbf{Y}_{\mathcal{P}}})$ nonzero columns of $\mathbf{U}\boldsymbol{\Lambda}^{1/2}$ such that $\mathbf{R}_{\mathbf{Y}_{\mathcal{P}}} = \mathbf{V}\mathbf{V}^{\dagger}$. Similarly, let the size $L \times r$ matrix $\mathbf{W}$ satisfy $\mathbf{R}_{\mathbf{X}} = \mathbf{W}\mathbf{W}^{\dagger}$. It follows that each row of $\mathbf{W}$ will contain nonzero entries if and only if the same holds for $\mathbf{R}_{\mathbf{X}}$—i.e., by identifying the nonzero rows of $\mathbf{W}$, the sector support $\mathcal{Q}$ is recovered. Thus, we seek to determine the unknown $\mathbf{W}$ from the available $\mathbf{V}$. Substituting these matrix factorizations into (17), we have

$$\mathbf{V}\mathbf{V}^{\dagger} = (\mathbf{F}_{\mathcal{P}}\mathbf{W})\,(\mathbf{F}_{\mathcal{P}}\mathbf{W})^{\dagger}. \tag{19}$$

Since $\mathbf{F}_{\mathcal{P}}$ is a $P \times L$ matrix with $P \leq L$, the $L \times P$ matrix $\mathbf{W}$ is not uniquely determined by the system

$$\mathbf{V} = \mathbf{F}_{\mathcal{P}}\mathbf{W}. \tag{20}$$

The CS problem seeks the solution $\hat{\mathbf{W}}$ that minimizes the number of rows having nonzero entries. This particular ℓ_0-minimization problem may be replaced by the computationally preferable (specifically, convex) ℓ_1-minimization problem. In this MMV setting, this can be accomplished using the mixed $\ell_{2,1}$ matrix norm

$$\|\mathbf{W}\|_{2,1} = \left(\sum_{i=0}^{L-1} \left\| \mathbf{w}^i \right\|_2 \right) \tag{21}$$

with $\mathbf{w}^i$ denoting the i th row of $\mathbf{W}$. The aim is then to solve the optimization problem

$$\hat{\mathbf{W}} = \underset{\mathbf{W}\in\mathbb{C}^{L\times r}}{\operatorname{argmin}} \|\mathbf{W}\|_{2,1} \text{ subject to } \mathbf{V} = \mathbf{F}_{\mathcal{P}}\mathbf{W}. \tag{22}$$

If the solution to (22) is unique, the recovered support $\hat{\mathcal{Q}}$ comprising the indices of the nonzero rows of $\hat{\mathbf{W}}$ will be correct and can be used in (13) to complete the image reconstruction. A sufficient condition guaranteeing a unique recovery is given by [15]

$$P \geq 2Q - \operatorname{rank}(\mathbf{R}_{\mathbf{X}}) + 1. \tag{23}$$

For a more detailed discussion of this formulation, and additional perspectives, see, e.g., [16]. More generally, there is a broader literature on algorithms for the solution of MMV problems; see, e.g., [15], [17].

The uniqueness condition of (23) tells us that the required number of cosets depends not only on the number of occupied sectors, but also upon the cross-correlation of the scene content among the different sectors (for example, due to multi-path). This implies that in the worst-case $(\operatorname{rank}(\mathbf{R}_{\mathbf{X}}) = 1)$ we may require $P \geq 2Q$ cosets, as compared with $P \geq Q$ when the sector support is known, as discussed in Section III-A. Hence, not knowing the sector support *a priori* can incur a factor of two increase in the minimum number of array elements required for successful image reconstruction. However, when for each ψ the rows of $\mathbf{X}(\psi)$ form a linearly independent set, $\mathbf{R}_{\mathbf{X}}$ has rank Q and it follows from (23) that $P \geq Q + 1$ cosets are sufficient for recovery. In this case, the price of needing to learn the sector support is the requirement of a single additional coset.

Solutions to the ℓ_1-minimization problem may still require more computation than may be practical in a dynamic imaging application. For such scenarios, a computationally less expensive solution is the alternative originally proposed in [14] based on the MUSIC direction finding algorithm [4]. The basic algorithm is as follows. In the absence of noise, the correlation matrix $\mathbf{R}_{\mathbf{Y}_{\mathcal{P}}}$ has Q of its P eigenvalues nonzero. Accordingly, the eigenvector matrix is partitioned as $\mathbf{U} = [\mathbf{U}_{\mathrm{S}}\, \mathbf{U}_{\mathrm{N}}]$, where the $P \times Q$ matrix $\mathbf{U}_{\mathrm{S}}$ contains the eigenvectors corresponding to the nonzero eigenvalues. These eigenvectors form an orthonormal basis for the range of the measurement matrix $\mathbf{F}_{\mathcal{P}\mathcal{Q}}$, traditionally referred to as the *signal subspace*. The orthogonal subspace spanned by the columns of the $P \times (P - Q)$ matrix $\mathbf{U}_{\mathrm{N}}$ is known as the *noise subspace*. In this scenario, the zero-valued eigenvalues associated with this subspace reflect the noise-free idealization. To determine the support, each of the L columns of $\mathbf{F}_{\mathcal{P}}$ is projected onto the noise subspace. The columns corresponding to the active sectors contained within the support $\mathcal{Q}$ lie in the orthogonal subspace spanned by $\mathbf{U}_{\mathrm{S}}$ and hence will have zero projection onto $\mathbf{U}_{\mathrm{N}}$. The recovered support $\hat{\mathcal{Q}}$ contains the indices of these columns. Thus, with $\mathbf{F}_{\mathcal{P}}$ and $\mathbf{U}$ expressed in terms of their columns via the notation $\mathbf{F}_{\mathcal{P}} = [\mathbf{f}_0\, \mathbf{f}_1\, \ldots\, \mathbf{f}_{L-1}]$ and $\mathbf{U} = [\mathbf{u}_0\, \mathbf{u}_1\, \ldots\, \mathbf{u}_{P-1}]$ (where the $\mathbf{u}_m$ are ordered by eigenvalue size), the algorithm evaluates the *null spectrum*

$$D_{\mathrm{MUSIC}}(q) = \sum_{m=Q}^{P-1} |\mathbf{f}_q^{\dagger}\mathbf{u}_m|^2, \quad q = 0, 1, \ldots, L-1 \tag{24}$$

and selects as $\hat{\mathcal{Q}}$ the values of q such that $D_{\mathrm{MUSIC}}(q) = 0$.

For the case in which $\operatorname{rank}(\mathbf{R}_{\mathbf{X}}) = Q$, the MUSIC approach is particularly attractive, being a polynomial-time algorithm satisfying the lower bound of (23)[14]. However, it is well-known that the MUSIC algorithm is unreliable in scenarios corresponding to the case in which $\mathbf{R}_{\mathbf{X}}$ is rank deficient [4]. For such cases, a hybrid MMV algorithm referred to as subspace-augmented MUSIC, which combines MUSIC with orthogonal matching pursuit techniques, may be used to more efficiently handle rank deficiencies [18]. For additional results on the relationship between traditional CS MMV algorithms, MUSIC, and the issue of rank may be found in, e.g., [19], [20].

1) System Implementation: While not shown in Fig. 3, the sector support $\hat{\mathcal{Q}}$ is recovered from $\mathbf{y}_{\mathcal{P}}[n]$ prior to the remaining steps of the reconstruction. For this recovery procedure, the required correlation matrix $\mathbf{R}_{\mathbf{y}_{\mathcal{P}}}$ can also be computed from the coset responses directly in the array domain according to [cf. Equation (16)]

$$[\mathbf{R}_{\mathbf{y}_{\mathcal{P}}}]_{lk} = \sum_n y_{p_l}[n]\, y_{p_k}^*[n]. \tag{25}$$

The estimated support $\hat{\mathcal{Q}}$ is then utilized in the remaining reconstruction steps.

C. Coset Period Selection Considerations

For a fixed aperture length corresponding to a standard array of N elements, the choice of the coset period L in the associated multi-coset array involves a tradeoff between conflicting objectives.

On one hand, the sector-wise density $\rho_{s,L} = Q/L$ of the scene decreases monotonically with increasing L, converging to the limiting scene density ρ_s. Hence, this favors choosing a large value for L, so that the sparsest possible array can be used.

On the other hand, as L increases, the number of coset periods $M = N/L$ decreases, causing imaging performance to suffer. This is due mainly to two reasons. First, the number of coset periods can be viewed as corresponding to the number of "snapshots" involved in estimating the scene support, and fewer snapshots means less noise averaging. Second, with a finite array aperture, targets in active sectors $\mathcal{Q}$ effectively "spill over" into neighboring inactive sectors, so that underlying sparsity corresponding to (6) is obscured. Moreover, this leakage is exacerbated as the sectors become narrower.

As will be discussed shortly, the support recovery and scene reconstruction algorithms can be made robust to the situation in which (6) is violated by the presence of noise in the inactive sectors. Furthermore, from the perspective of the associated processing, the signal energy leaked into inactive sectors behaves like other sources of noise in the system. Hence, its dominant effect is to increase the noise floor in the measurements, and its impact can be neglected provided its level is significantly lower than that due to the combination of other sources of noise in the system. In practice, we can usually choose L small enough to ensure this.

More generally, the use of standard low-sidelobe tapers from the array processing literature will mitigate the spillover effect and help to make possible the use of larger values of L and thus sparser array designs at high SNRs. And for scenarios where leakage simply cannot be ignored, a refined version of the array-domain image reconstruction process is described in [5]. Using this aperture-aware reconstruction, it is shown that the finite-aperture effects may be reduced to any desired level by dedicating a suitable portion of the array to the task, which in turn incurs a corresponding reduction in resolution.

IV. MULTI-COSET ARRAY PROCESSING

Having summarized the basic principles and techniques governing multi-coset imaging, as the main contribution of the paper we now turn to the detailed design of robust multi-coset array processing.

Central to our development is quantifying the impact of noise on the performance of the imaging system, and identifying how to best mitigate it. Since noise affects both support recovery and scene reconstruction phases of the imaging process, we consider each separately, starting with the latter.

A. Reconstruction Noise Amplification

With respect to scene reconstruction, the second phase of the imaging process, noise causes a direct degradation in the reconstruction SNR (RSNR). In this section, we characterize the relationship between the SNR at the sensor and the resulting RSNR. Since the SNR at the sensor is the reconstruction SNR for a standard array, this relationship allows us to assess the impact of the multi-coset architecture. We focus on the high SNR regime, where we can assume the support is reliably recovered.

We begin by relating RSNR to the condition number of the relevant measurement matrix $\kappa(\mathbf{F}_{\mathcal{PQ}})$. First, let $x[n]$ denote the array response from the scene as before, but now we let $z[n]$ denote the spatially-white array response due to the noise. Defining $\mathbf{Z}(\psi) \in \mathbb{C}^L$ such that $[\mathbf{Z}(\psi)]_q = Z(\psi + q/L)$ is the associated coset response in the image domain, we then have

$$\mathbf{Y}_{\mathcal{P}}(\psi) = \mathbf{F}_{\mathcal{P}}(\mathbf{X}(\psi) + \mathbf{Z}(\psi)) = \mathbf{F}_{\mathcal{PQ}}\mathbf{X}_{\mathcal{Q}}(\psi) + \mathbf{F}_{\mathcal{P}}\mathbf{Z}(\psi). \tag{26}$$

Applying our scene reconstruction procedure (which ignores the noise), we obtain that the resulting noisy reconstruction is

$$\hat{\mathbf{X}}_{\mathcal{Q}}(\psi) = \mathbf{F}^{+}_{\mathcal{PQ}}\mathbf{Y}_{\mathcal{P}}(\psi) = \mathbf{X}_{\mathcal{Q}}(\psi) + \mathbf{F}^{+}_{\mathcal{PQ}}\mathbf{F}_{\mathcal{P}}\mathbf{Z}(\psi) \tag{27}$$

which corresponds to the desired image plus an amplified noise component.

The reference noise level is

$$N_0 \triangleq \mathbb{E}\left[\int_0^1 |Z(\psi)|^2 \,\mathrm{d}\psi\right] \tag{28}$$

which corresponds to the reconstruction noise level in a standard array. For the multi-coset array, the reconstruction noise level is, via (27),

$$\begin{aligned} N_r &= \mathbb{E}\left[\int_0^1 \|\mathbf{F}^{+}_{\mathcal{PQ}}\mathbf{F}_{\mathcal{P}}\mathbf{Z}(\psi)\|_2^2 \,\mathrm{d}\psi\right] && (29)\\ &= \mathrm{Tr}\left((\mathbf{F}^{+}_{\mathcal{PQ}}\mathbf{F}_{\mathcal{P}})\mathbb{E}\left[\mathbf{R}_Z\right](\mathbf{F}^{+}_{\mathcal{PQ}}\mathbf{F}_{\mathcal{P}})^{\dagger}\right) && (30)\\ &= \mathrm{Tr}\left(\mathbf{F}^{+}_{\mathcal{PQ}}\mathbf{F}_{\mathcal{P}}\mathbf{F}^{\dagger}_{\mathcal{P}}\mathbf{F}^{+,\dagger}_{\mathcal{PQ}}\right)\frac{N_0}{L} && (31)\\ &= \mathrm{Tr}\left(\mathbf{F}^{+}_{\mathcal{PQ}}\mathbf{F}^{+,\dagger}_{\mathcal{PQ}}\right)\frac{N_0}{L^2} && (32) \end{aligned}$$

where in (30) $\mathrm{Tr}(\cdot)$ denotes the trace operator, where to obtain (31) we have use the spatial whiteness of $z[n]$, and where to obtain (32) we have used that the rows of $\mathbf{F}_{\mathcal{P}}$ are taken from the $L \times L$ (inverse) DFT matrix, whence $\mathbf{F}_{\mathcal{P}}\mathbf{F}^{\dagger}_{\mathcal{P}} = \mathbf{I}/L$ with $\mathbf{I}$ denoting the identity matrix.

Comparing (28) with (32), and recognizing that

$$\|\mathbf{A}\|_{\mathrm{F}}^2 \triangleq \mathrm{Tr}(\mathbf{A}\mathbf{A}^{\dagger})$$

is the squared Frobenius norm of an arbitrary matrix $\mathbf{A}$[21], we see that the RSNR in the multi-coset imaging system is reduced by a factor

$$\begin{aligned} \frac{N_r}{N_0} &= \frac{\|\mathbf{F}^{+}_{\mathcal{PQ}}\|_{\mathrm{F}}^2}{L^2}\\ &= \frac{1}{L^2}\sum_{j=0}^{P-1}\sum_{i=0}^{Q-1}\left|\left[\mathbf{F}^{+}_{\mathcal{PQ}}\right]_{ij}\right|^2\\ &= \frac{1}{L^2}\sum_{i=0}^{Q-1}\left|\sigma_i(\mathbf{F}^{+}_{\mathcal{PQ}})\right|^2\\ &= \frac{1}{L^2}\sum_{i=0}^{Q-1}\frac{1}{|\sigma_i(\mathbf{F}_{\mathcal{PQ}})|^2} && (33) \end{aligned}$$

where the $\{\sigma_i(\mathbf{F}^{+}_{\mathcal{PQ}})\}$ are the Q nonzero singular values of $\mathbf{F}^{+}_{\mathcal{PQ}}$, and where to obtain (33) we have used that the singular values of a matrix are the reciprocals of the singular values of its pseudo-inverse.

In the high SNR regime, the condition number of the measurement matrix, $\kappa(\mathbf{F}_{\mathcal{PQ}})$, which is the ratio of its maximum to minimum singular values, accurately reflects the degree of noise amplification in the reconstruction. To see this, note that since $\mathbf{F}_{\mathcal{PQ}}$ is a $P \times Q$ matrix with each entry having magnitude $1/L$, it follows that

$$\|\mathbf{F}_{\mathcal{PQ}}\|_{\mathrm{F}}^2 = \sum_{i=0}^{Q-1}|\sigma_i(\mathbf{F}_{\mathcal{PQ}})|^2 = \frac{PQ}{L^2}. \tag{34}$$

Thus, while the sum in (34) is fixed for a given L, P, and Q, the sum in (33) may vary greatly, depending on the distribution of the singular values of the measurement matrix. Specifically, the smaller the minimum $\sigma_i(\mathbf{F}_{\mathcal{PQ}})$, the larger the noise amplification. Hence, in the selection of the coset pattern, it is desirable to select $\mathcal{P}$ such that $\kappa(\mathbf{F}_{\mathcal{PQ}})$ takes relatively small values for *all* support sets $\mathcal{Q}$.

We note too that when the noise level is known a priori, the reconstruction procedure can be modified to take it into account, via, e.g., a minimum mean-square error estimation formulation.

Due to space constraints, we do not develop this generalization here, but remark that this leads to improved RSNR.

B. Support Recovery Reliability

With respect to support recovery, the first phase of the imaging process, the presence of noise means that (6) does not strictly hold for any $Q < L$, and thus there is no exact sparse solution to (11). As a result, modifications to the support recovery algorithm are required. Ultimately, we characterize the performance of the support recovery phase in terms of the threshold SNR (TSNR) above which the correct support $\mathcal{Q}$ can be reliably recovered with high probability, and note that this threshold will in general depend on the scene density and choice of coset pattern $\mathcal{P}$.

Before characterizing the support recovery performance, we first develop how to accommodate noise in the both the ℓ_1-minimization and MUSIC-based approaches to the problem.

With respect to the ℓ_1-minimization approach, we note that the optimization (22) must be modified. In particular, following standard practice, since the noise precludes the possibility of an exact sparse solution, we relax the equality constraint in (22), yielding

$$\hat{\mathbf{W}} = \underset{\mathbf{W}\in\mathbb{C}^{L\times r}}{\operatorname{argmin}} \|\mathbf{W}\|_{2,1} \text{ subject to } \|\mathbf{V} - \mathbf{F}_{\mathcal{P}}\mathbf{W}\|_{\mathrm{F}}^2 < \epsilon \quad (35)$$

where ϵ is chosen as a function of the SNR. A variety of algorithms suited to this noisy MMV problem can be found in, e.g., [22], [23].

For the MUSIC algorithm approach, the extension to the noisy case is straightforward when the number of measurements is large enough such that the eigenvector matrix $\mathbf{U}$ has converged to roughly the noise free case, and the noise power is uniformly distributed throughout both the signal and noise subspaces [4]. However, difficulties arise when the number of coset periods is more limited. In particular, $\mathbf{U}_{\mathrm{S}}$ and $\mathbf{U}_{\mathrm{N}}$ will not accurately partition the signal and noise subspaces, and the contribution due to noise is no longer evenly distributed over the P eigenvalues.

A "soft" version of the MUSIC algorithm known as the eigenvalue method [24] accounts for finite sample sets by weighing the projections onto each subspace direction $\mathbf{u}_m$ more heavily for smaller eigenvalues. Specifically, the null-spectrum under this method is given by

$$D_{\mathrm{EV}}(q) = \sum_{m=Q}^{P-1} \frac{1}{\lambda_m} |\mathbf{f}_q^{\dagger}\mathbf{u}_m|^2 \quad (36)$$

where the eigenvalues λ_m are the (ordered) diagonal elements of $\mathbf{\Lambda}$. In essence, this approach aims to suppress the signal contribution within the estimate of $\mathbf{U}_{\mathrm{N}}$ in order to obtain a more accurate representation of the true noise subspace.

At low SNR, as the threshold between signal and noise eigenvalues becomes less distinct, the estimated signal eigenvectors can potentially be aligned more closely to the true noise subspace than the true signal subspace. This point is unaccounted for in (36). Based on this observation, we have found the still "softer" version of MUSIC, corresponding to the null-spectrum

$$D_{\mathrm{MEV}}(q) = \sum_{m=0}^{P-1} \left(\frac{1}{\lambda_m^{1/2}} - \frac{1}{\lambda_0^{1/2}} \right)^2 |\mathbf{f}_q^{\dagger}\mathbf{u}_m|^2 \quad (37)$$

to be effective at low SNR—a regime in which MUSIC has traditionally been considered unsuitable. We stress that this version of MUSIC includes contributions from the *entire* column space of $\mathbf{U}$, save for the eigenvector associated with the largest eigenvalue λ_0.

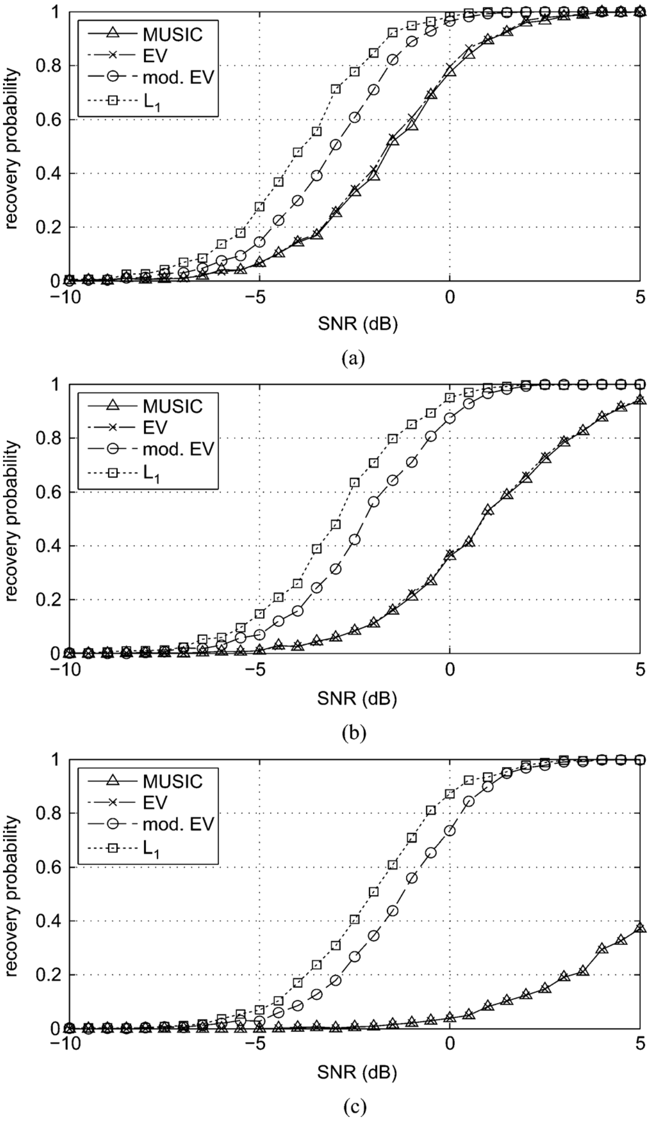

(a)

(b)

(c)

Fig. 4. Empirical recovery probability versus SNR for the MUSIC (24), eigenvalue-MUSIC (36), modified-eigenvalue-MUSIC (37), and ℓ_1-minimization (35) algorithms, with $L = 19$, $P = 9$, and (a) $Q = 6$ (b) $Q = 7$ (c) $Q = 8$.

Numerical simulations were performed to compare the different recovery algorithms. A representative example of the results is shown in Fig. 4. In these simulations, a coset period of $L = 19$ with $P = 9$ active cosets was selected. The coset pattern is fixed at $\mathcal{P} = \{0, 1, 2, 3, 5, 7, 12, 13, 16\}$, selected by the design algorithm to be described in the next section. To gauge the recovery performance of the basic MUSIC, eigenvalue-MUSIC (soft MUSIC), modified-eigenvalue-MUSIC (softer MUSIC), and ℓ_1-minimization algorithms, each was applied to 1000 randomly generated scenes in which $Q = 7, 8,$ and 9 active sectors supported by $\mathcal{Q}$ were selected at random. Gaussian noise was added to each scene, evenly distributed over the entire range of ψ. This was repeated over a range of SNRs. A successful recovery was declared when the Q most likely active sectors as estimated by the respective algorithm matched exactly to the Q sectors contained in $\mathcal{Q}$. While the ℓ_1 algorithm gave the best result, our modified MUSIC algorithm performed nearly as well, reaching a recovery probability of nearly 100% at a similar TSNR, while requiring considerably less computation time. The most striking result is the notable improvement beyond the established MUSIC algorithms.

V. MULTI-COSET ARRAY PATTERN DESIGN

We now develop the design of good multi-coset array patterns over a linear aperture of length N measured in half-wavelengths. In our development, we assume the coset period L has been chosen based on the considerations in Section III-C. This means that scenes of a given density are characterized by a particular value of Q, which we treat as known. For this scenario, we consider array designs with density corresponding to a number of active cosets P such that $P \geq Q+1$, consistent with our earlier development, but note that in practice the addition of at least one additional coset (i.e., $P \geq Q+2$) provides large performance gains in support recovery.

In our development, we pursue the design of (P, L) multi-coset array patterns that are uniformly good for all (Q, L)-sparse scenes, and separately consider the high and low SNR regimes.

A. High SNR Designs

At high SNR, the correct support is recovered with high probability, so system performance is largely determined by the RSNR achieved during the scene reconstruction phase of imaging. Based on the analysis in Section IV-A, which reveals that the performance is dominated by the smallest eigenvalue of the measurement matrix $\mathbf{F}_{\mathcal{PQ}}$, we seek the coset pattern $\mathcal{P}$ of size $|\mathcal{P}| = P$ such that the measurement matrix $\mathbf{F}_{\mathcal{PQ}}$ remains well conditioned for all possible supports $\mathcal{Q}$ satisfying $|\mathcal{Q}| \leq Q$, i.e.,

$$\mathcal{P}^*_\kappa = \underset{\mathcal{P} \in \mathcal{C}_P}{\operatorname{argmin}} \max_{\mathcal{Q} \in \mathcal{C}_Q} \kappa\left(\mathbf{F}_{\mathcal{PQ}}\right). \tag{38}$$

Note, however, that the sets $\mathcal{C}_P$ and $\mathcal{C}_Q$ containing the possible choices of $\mathcal{P}$ and $\mathcal{Q}$ grow rapidly with increasing L. An exhaustive search based on (38) requires $|\mathcal{C}_P| \cdot |\mathcal{C}_Q|$ calculations of $\kappa(\mathbf{F}_{\mathcal{PQ}})$, which makes this conceptually straightforward design approach largely impractical from the perspective of computational complexity.

B. Low SNR Designs

At lower SNR, errors in the support recovery become significant, and thus system performance is determined more by the TSNR achieved during the support recovery phase of imaging. In this regime, the design procedure in Section V-A that tackles the condition number of the induced measurement matrix $\mathbf{F}_{\mathcal{PQ}}$ is less meaningful. Instead, in this low SNR regime, we develop an alternate design framework that strives to improve the estimation of the correlation matrix $\mathbf{R_X}$ used for support recovery (recall e.g., (22)).

Consider the correlation matrix associated with all L cosets

$$\mathbf{R_Y} = \mathbf{F}\mathbf{R_X}\mathbf{F}^\dagger. \tag{39}$$

For the moment, assume uncorrelated scene sectors, i.e.,

$$[\mathbf{R_X}]_{mn} = \int_0^{1/L} X_m(\psi)\, X_n^*(\psi)\, \mathrm{d}\psi = \begin{cases} \sigma_m^2 & m = n \\ 0 & m \neq n \end{cases} \tag{40}$$

where $\sigma_m^2 = \int_0^{1/L} |X_m(\psi)|^2\, \mathrm{d}\psi$ is the signal energy from sector m. In this case, the full correlation matrix has a Hermitian-circulant structure

$$[\mathbf{R_Y}]_{lk} = \frac{1}{L^2} \sum_{q=0}^{L-1} \sigma_q^2 e^{j2\pi(l-k)q/L}. \tag{41}$$

From (41), the dependence of the matrix entries on the relative spacing between elements indicates the importance of the pairwise spacings as represented by the $2(L-1)$ off-diagonals. Specifically, the information contained in $\mathbf{R_Y}$ can be obtained by representing each of the possible spacings a single time. The symmetries in the Hermitian-circulant structure reduce the number of unknowns by another factor of four, suggesting the entire matrix could be represented by only $\lceil (L-1)/2 \rceil$ unknowns.

Clearly, each of these unknowns can be estimated if and only if the coset pattern includes the corresponding element spacing. In particular, we start by defining the following modulo-distance between pairs of elements l, k within a single coset period:

$$t_{lk} \triangleq \min\{|l-k|, L-|l-k|\}. \tag{42}$$

In turn, we count the number of times each pairwise spacing is found in a particular pattern $\mathcal{P}$. For this purpose, the *co-array weight* of $\mathcal{P}$ is a vector of the number of times each modulo-distance occurs in the pattern. In particular, the t th entry of $\mathcal{P}$ is the number of times the distance t occurs, i.e.,

$$[\mathbf{c}_\mathcal{P}]_t \triangleq \sum_{\{(l,k): t_{lk} = t\}} s_l s_k, \quad 1 \leq t \leq \frac{L-1}{2} \tag{43}$$

where $\mathbf{s}_\mathcal{P}$ is the binary selection vector with entries

$$[\mathbf{s}_\mathcal{P}]_l = \begin{cases} 1, & l \in \mathcal{P} \\ 0, & \text{otherwise,} \end{cases} \qquad l = 0, 1, \ldots, L-1. \tag{44}$$

Now, if we choose just enough elements s.t. the weight vector $\mathbf{c}_\mathcal{P}$ has no zeros, we can have (in the ideal setting) the complete $\mathbf{R_Y}$. The resulting pattern design problem is similar to Minimum Redundancy Linear Arrays (MRLA), introduced in [25], where the goal is to design an array where the number of occurrences of different spacings is uniform. Indeed, The weight vector $\mathbf{c}_\mathcal{P}$ can be viewed as a modulo version of the co-array originally defined in [25]. In a recent work [6] a similar problem is addressed from a different perspective. A systematic way to produce "almost MRLA" designs was introduced, showing that for large L the number of elements required is in the order of $\sqrt{L}$.

Now, for a sparse scene we may not need to estimate the full $\mathbf{R_Y}$, and the number of cosets required may be smaller than that required for the MRLA design. On the other hand, imperfections such as noise and correlation may require more elements. It seems reasonable to still keep the design fairly "balanced",

TABLE I
EXAMPLES OF COSET PATTERNS $\mathcal{P}_c^*$ SELECTED ACCORDING TO THE CO-ARRAY APPROACH.

L	P	ρ_A	$\mathcal{P}_c^*$	c^*
7	3	0.43	$\{0\,1\,3\}$	1
7	4	0.57	$\{0\,1\,2\,4\}$	2
11	5	0.45	$\{0\,1\,2\,4\,7\}$	2
11	6	0.55	$\{0\,1\,2\,4\,5\,7\}$	3
13	4	0.31	$\{0\,1\,3\,9\}$	1
13	9	0.69	$\{0\,1\,2\,3\,4\,5\,7\,9\,10\}$	6
19	9	0.47	$\{0\,1\,2\,3\,5\,7\,12\,13\,16\}$	4
19	10	0.53	$\{0\,1\,2\,3\,5\,7\,12\,13\,15\,16\}$	5

TABLE II
MAXIMUM CONDITION NUMBERS, $Q = P - 1$.

L	P	$\kappa^{\max}_{\mathcal{P}^*_\kappa}$	$\kappa^{\max}_{\mathcal{P}^*_c}$	$\kappa^{\max}_{\mathcal{P}_\mathrm{b}}$
7	3	1.31	1.66	2.64
7	4	2.18	2.18	3.60
11	5	4.24	4.24	17.54
11	6	5.17	5.17	20.22
13	4	2.75	3.26	15.85
13	9	6.49	6.49	33.25
19	9	13.54	13.54	1063.63
19	10	13.93	13.93	1154.08

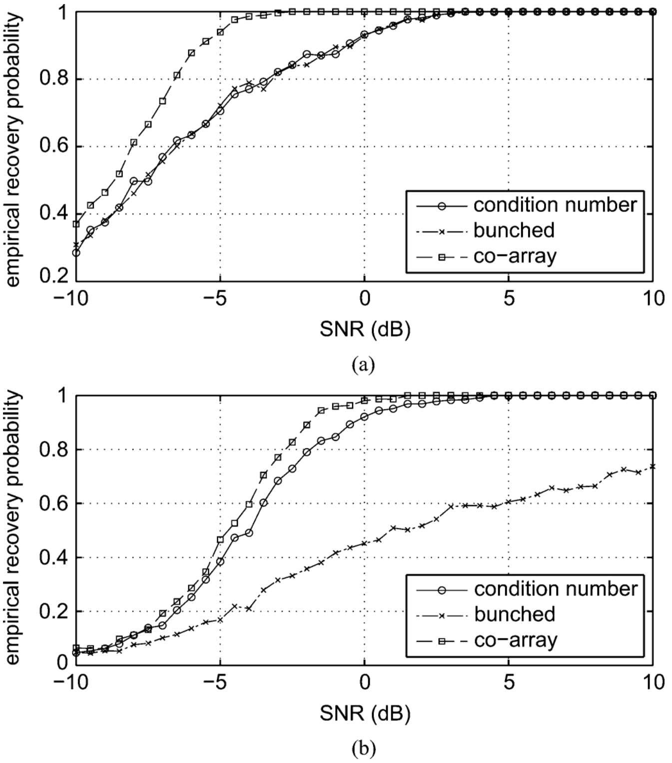

Fig. 5. Recovery probability versus SNR for (a) $(L, P, Q) = (7, 3, 2)$ and (b) $(L, P, Q) = (13, 4, 3)$.

i.e., to use a design that keeps $\mathbf{c}_\mathcal{P}$ fairly balanced. This can be computed by selecting the coset pattern having the co-array $\mathbf{c}_\mathcal{P}$ with the smallest ℓ_2-norm, i.e.,

$$\mathcal{P}_c^* = \underset{\mathcal{P} \in \mathcal{C}_P}{\operatorname{argmin}} \|\mathbf{c}_\mathcal{P}\|_2. \tag{45}$$

C. Pattern Computation, Evaluation, and Comparison

A quick comparison of (38) and (45) shows that the co-array based design approach entails significantly fewer computations due to the independence of this design on $\mathcal{Q}$. In this section, we show that the co-array designs are also optimal—or very close to optimal—in performance in both low and high SNR regimes.

To begin, we examine a set of (L, P) pairs for which the number of unique element pairs $P(P-1)/2$ is an integer multiple of the number of possible spacings $(L-1)/2$. This condition makes it possible, in principle, for a pattern to have a perfectly flat co-array distribution: each entry of $\mathbf{c}_\mathcal{P}$ takes the identical value $c^* = P(P-1)/(L-1)$. Examples of coset patterns fitting this description are shown in Table I, along with the array density ρ_A, and the associated value of c^*.

Focusing on the $(4, 7)$-sparse array in this table for purposes of illustration, note first that this array layout is depicted in Fig. 1. We emphasize, too, that this coset pattern can be used with any number of coset periods M depending on the array length, and that the effective array density is approximately 57% of the number of elements contained in a standard array of the same length. The corresponding co-array is $\mathbf{c}_\mathcal{P} = [2\,2\,2]$, which reflects that there are two element pairs having each of the (modulo) spacings 1 (element pairs $(0, 1)$ and $(1, 2)$), 2 (element pairs $(0, 2)$ and $(2, 4)$), and 3 (element pairs $(1, 4)$ and $(0, 5)$).

For the values of L and P shown in Table I, it is computationally feasible to determine the condition number of the measurement matrix $\kappa(\mathbf{F}_{\mathcal{P}\mathcal{Q}})$ over the sets $\mathcal{C}_P$ and $\mathcal{C}_Q$, corresponding to the high SNR regime design framework. From these results, the maximum condition number $\kappa^{\max}_\mathcal{P}$ over all $\mathcal{Q}$ of length $Q = P - 1$ is determined for each $\mathcal{P}$. The worst-case condition numbers for the high SNR design ($\kappa^{\max}_{\mathcal{P}^*_\kappa}$), low SNR design ($\kappa^{\max}_{\mathcal{P}^*_c}$), and bunched pattern design ($\kappa^{\max}_{\mathcal{P}_\mathrm{b}}$) are shown in Table II for each of the (L, P) pairs in Table I. The bunched pattern $\mathcal{P}_\mathrm{b} = \{0, 1, \ldots, P-1\}$, mentioned in Section III-A, is included for reference as an example of a universal pattern that guarantees only that the measurement matrix will have a finite condition number for all $\mathcal{Q}$.

As an initial observation, note that the bunched patterns lead to poor RSNR performance, as we would expect. Next, note that there are many entries in Table II for which $\kappa^{\max}_{\mathcal{P}^*_\kappa}$ and $\kappa^{\max}_{\mathcal{P}^*_c}$ match, revealing that our high SNR and low SNR designs often yield identical patterns. Moreover, even when they differ, our low SNR designs do not sacrifice significant RSNR performance when used in the high SNR regime. Hence, we conclude that even at high SNR, the co-array based pattern designs are at least "near" optimal.

Conversely, we can also evaluate the performance of our high SNR designs in the low SNR regime in the two instances in Table II where the designs differ from their low SNR counterparts. In particular, in Fig. 5 we plot the recovery probability as a function of SNR for the $(3, 7)$ and $(4, 13)$ sparse arrays. In this case, we see that these high SNR designs offer conspicuously poorer TSNR performance in the low SNR regime.

Equally noteworthy, with these and all other choices of (P, L) for which simulations were conducted, the co-array pattern designs consistently yielded the lowest TSNR for reliable support recovery among all possible patterns, providing additional evidence that co-array based pattern design framework is well matched to the low SNR regime.

TABLE III
EXAMPLES OF COSET PATTERNS $\mathcal{P}_c^*$ FOUND USING MCMC.

L	P	ρ_A	$\mathcal{P}_c^*$	c^*
21	5	0.24	$\{0\,1\,6\,8\,18\}$	1
21	16	0.76	$\{0\,1\,2\,3\,4\,5\,6\,7\,8\,10\,12\,13\,14\,15\,18\,19\}$	12
23	11	0.48	$\{0\,1\,2\,3\,5\,7\,8\,11\,12\,15\,17\}$	5
23	12	0.52	$\{0\,1\,2\,3\,4\,6\,8\,9\,12\,13\,16\,18\}$	6
31	6	0.19	$\{0\,1\,14\,20\,24\,29\}$	1
31	15	0.48	$\{0\,1\,2\,3\,5\,7\,11\,14\,15\,16\,22\,23\,26\,28\,29\}$	7
31	16	0.52	$\{0\,1\,2\,3\,4\,6\,7\,8\,12\,14\,16\,17\,19\,24\,25\,28\}$	8
35	17	0.49	$\{0\,1\,2\,3\,5\,6\,10\,16\,17\,18\,22\,24\,25\,27\,28\,31\,33\}$	8
37	9	0.24	$\{0\,1\,3\,9\,13\,14\,21\,31\,35\}$	2
57	8	0.14	$\{0\,1\,13\,15\,21\,24\,31\,53\}$	1

While co-array based designs offer attractive performance characteristics, for coset periods beyond $L = 20$, the exhaustive search for such patterns via (45) over $\mathcal{C}_P$ consumes significant computation. In this regime, it is natural to replace the brute force search with an iterative optimization based on the Markov Chain Monte Carlo (MCMC) method [26]. In our experiments, we found this approach effective for quickly determining well designed coset patterns. Several examples with uniform co-arrays obtained from this procedure are shown in Table III.

It is important to emphasize that while the coset pattern examples shown in Tables I and III can be considered "perfect" in the sense of our co-array metric, the set of patterns that are good in a practical sense is considerably larger. Indeed, small deviations from a uniform co-array generally do not significantly impact performance. Consequently, within the process of selecting $\mathcal{P}$, emphasis should be placed on arriving at a pattern for which the elements of $\mathbf{c}_{\mathcal{P}}$ are distributed in a reasonably even fashion. In the simulations of Section VII, we use such a "near-perfect" pattern for a scenario with parameters $L = 47$ and $P = 28$.

VI. SUPPORT RECOVERY FAILURE DETECTION

In practice, the scene density and SNR may not be known in advance, or may evolve dynamically. As we have shown, both these quantities affect the support recovery reliability in a multi-coset array imaging system. While we could choose the number of cosets in our array to cover a worst-case scenario, in the typical case this would be rather wasteful of resources. An alternative to such an approach would be to use considerably less overprovisioning, and instead develop a method for detecting when the scene density exceeds the level at which a reliable image can be formed.

In this section, we develop such an approach. And while methods can be developed for detecting such false images at high levels of abstraction using machine vision techniques, in our development we focus on the use of low-level techniques that can be easily integrated into our array processing pipeline.

The technique we develop is based on the concept of *back-projection error* (BPE). Consider the (P, L) multi-coset array with coset pattern $\mathcal{P}$ and a (Q, L)-sparse scene with support $\mathcal{Q}$, where both Q and $\mathcal{Q}$ are unknown. In the support recovery stage, the received information contained in $\mathbf{Y}_{\mathcal{P}}(\psi)$ is used to obtain an estimate of the support $\hat{\mathcal{Q}}$. Using the estimated support, the image is reconstructed as $\hat{\mathbf{X}}_{\hat{\mathcal{Q}}}(\psi) = \mathbf{F}^+_{\mathcal{P}\hat{\mathcal{Q}}}\mathbf{Y}_{\mathcal{P}}(\psi)$. Since the true $\mathbf{X}_{\mathcal{Q}}(\psi)$ is unknown, we use a *back-projection* onto the space spanned by $\hat{\mathcal{Q}}$ for comparison to the original coset response

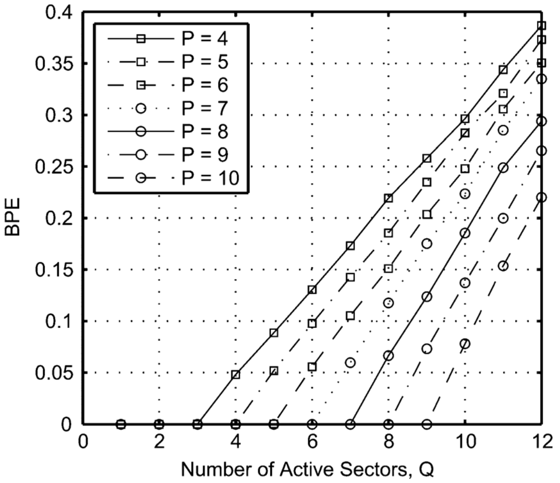

Fig. 6. BPE versus Q, $L = 19$. Results averaged over 1000 trials.

$$\hat{\mathbf{Y}}_{\mathcal{P}\hat{\mathcal{Q}}}(\psi) = \mathbf{F}_{\mathcal{P}\hat{\mathcal{Q}}}\hat{\mathbf{X}}_{\hat{\mathcal{Q}}}(\psi) = \mathbf{F}_{\mathcal{P}\hat{\mathcal{Q}}}\mathbf{F}^+_{\mathcal{P}\hat{\mathcal{Q}}}\mathbf{Y}_{\mathcal{P}}(\psi). \tag{46}$$

Where the product $\mathbf{F}_{\mathcal{P}\hat{\mathcal{Q}}}\mathbf{F}^+_{\mathcal{P}\hat{\mathcal{Q}}}$ is the projection matrix onto the range of $\mathbf{F}_{\mathcal{P}\hat{\mathcal{Q}}}$.

If $\hat{\mathcal{Q}}$ is correct, the back-projection $\hat{\mathbf{Y}}_{\mathcal{P}\hat{\mathcal{Q}}}(\psi)$ should be approximately equal to $\mathbf{Y}_{\mathcal{P}}(\psi)$, provided the noise level is relatively low. We quantify this through the back-projection error,

$$\mathrm{BPE} = \int_0^{1/L} \|\mathbf{Y}_{\mathcal{P}}(\psi) - \hat{\mathbf{Y}}_{\mathcal{P}\hat{\mathcal{Q}}}(\psi)\|_2^2 \, \mathrm{d}\psi. \tag{47}$$

A. Failure Detection in the Absence of Noise

Consider first the case where the noise level is negligible relative to the received signal power. As discussed in Section III, a multi-coset array with a (P, L)-universal pattern should be able to recover the support $\mathcal{Q}$ of a (Q, L)-sparse scene in most cases given $P \geq Q + 1$. When the support estimate recovered from the response $\mathbf{Y}_{\mathcal{P}}(\psi) = \mathbf{F}_{\mathcal{P}\mathcal{Q}}\mathbf{X}_{\mathcal{Q}}(\psi)$ is (or contains) the correct support such that $\mathcal{Q} \subseteq \hat{\mathcal{Q}}$, the back-projection is

$$\hat{\mathbf{Y}}_{\mathcal{P}\hat{\mathcal{Q}}}(\psi) = \mathbf{F}_{\mathcal{P}\hat{\mathcal{Q}}}\hat{\mathbf{X}}_{\hat{\mathcal{Q}}}(\psi) = \mathbf{F}_{\mathcal{P}\mathcal{Q}}\mathbf{X}_{\mathcal{Q}}(\psi) = \mathbf{Y}_{\mathcal{P}}(\psi) \tag{48}$$

and the BPE is zero. When the scene is insufficiently sparse for the array, the recovery stage fails to determine the entirety of the support and $\hat{\mathcal{Q}} \subset \mathcal{Q}$. In this case, much of the energy contained in the unidentified support sectors $\mathcal{Q}/\hat{\mathcal{Q}}$ vanishes during the back-projection operation. This behavior can be seen in Fig. 6. Each curve represents a fixed number of cosets P for which the average BPE is plotted as a function of the number of supported sectors Q. The average BPE was calculated over 1000 trials, each trial having a random Gaussian scene evenly distributed over a randomly selected support $\mathcal{Q}$. As expected, each curve remains at zero for $Q < P$ and rises in nearly linear fashion with Q beyond this point.

B. Failure Detection in the Presence of Noise

To understand how the presence of noise impacts the BPE, consider a scene with fixed signal power distributed over any

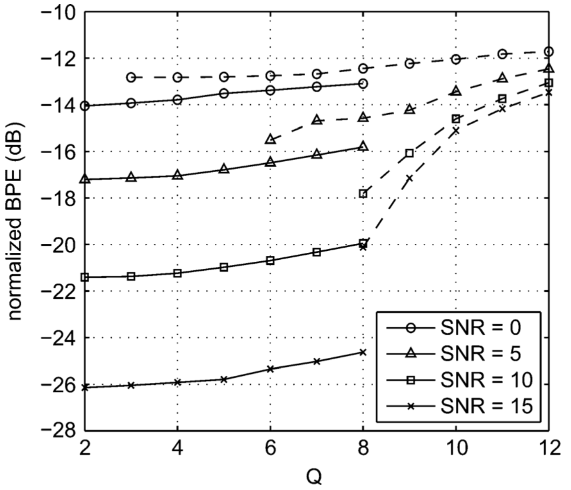

Fig. 7. Normalized BPE versus Q, at different SNR, $L = 19$, $P = 9$. The solid and dashed portion of each curve represent the successful and failed cases, respectively.

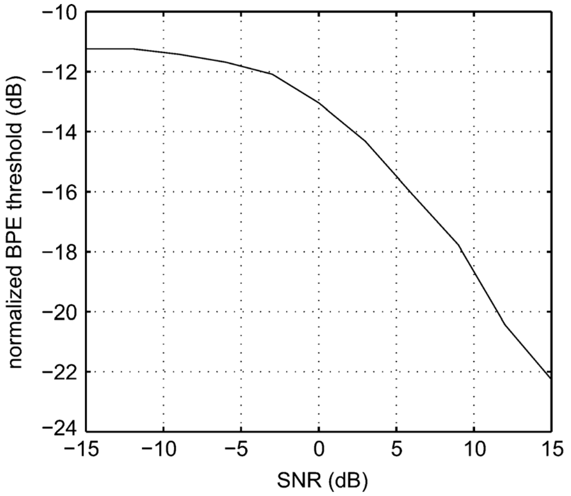

Fig. 8. Normalized BPE threshold versus SNR, $L = 19$, $P = 9$.

$Q \leq P - 1$ sectors. For noise powers below some threshold level (specific to the particular values of L, Q, and $\mathcal{P}$), the support recovery will not be adversely affected. In this region, the support $\mathcal{Q}$ will be recovered successfully and the BPE will be due solely to the noise within the subspace orthogonal to the range of $\mathbf{F}_{\mathcal{PQ}}$, which will increase in proportion to the total noise power. As a consequence, failures occur with increasing likelihood for $P > Q$ at lower SNRs. Hence, a useful failure detection mechanism is to indicate when the BPE exceeds some prescribed threshold.

The choice of this threshold depends on SNR, as Fig. 7 reflects. This figure shows the normalized BPE versus Q for different SNR values for a $(9, 19)$ multi-coset array. Rather than averaging the BPE results over every trial as in Fig. 6, the averages are instead taken separately for the cases of successful and failed support recovery estimates. We observe that independent of Q, the failed cases consistently lie above some threshold, which varies with SNR. Defining the threshold BPE as the midpoint between the maximum success and minimum failure BPEs allows a nominal level indicating a probable failure to be determined at each SNR. Fig. 8 illustrates the resulting BPE thresholds from this analysis for the $(9, 19)$ array. Similar analysis can be undertaken for any other particular array pattern, providing a general approach for calibration of the BPE.

VII. RANGE-AZIMUTH 2-D IMAGING SIMULATIONS

In this section, the multi-coset imaging techniques of the paper are applied to create a two-dimensional range-azimuth image from simulated data. In our development, we first develop the extension of our framework to scenes with range-dependent sparsity, which is more commonly experienced in applications.

A. Range-Dependent Scene Sparsity

While many scenes are not strictly sparse when viewed solely in terms of azimuthal sectors of arbitrary range, they are often sparse in azimuth when further partitioned into range cells. In active systems, such range partitioning can be achieved through the use of standard pulse compression techniques. This suggests a natural architecture where pulse compression is used to sort content into range cells, after which our multi-coset imaging techniques are applied separately at each range.

Pulse compression techniques are well understood, and many good treatments are available in the literature. For our purposes, it suffices to keep in mind the following characteristics. For a transmitted waveform containing a range of frequencies Δf about the center frequency f_0, the inverse Fourier transform of the received frequency domain data sorts the response according to the two-way travel times of the various signals reflected from the environment. In a typical medium, each of these signals travel at the same speed, hence sorting by time effectively sorts by distance.

From this perspective, the pulse-compressed range resolution improves linearly with the bandwidth Δf. As the scene is divided into finer range cells, the resultant range-dependent sparsity profile improves, since the density at any range is monotonically non-increasing as the range cell length Δr decreases. The available *fractional* bandwidth $\Delta f / f_0$ of a particular array design is relatively fixed for any f_0. Hence, exploitation of range-dependent sparsity is inherently well suited for high frequency systems. This is the model we use in our simulations.

B. 2-D Imaging Illustration

As a demonstration of multi-coset range-azimuth imaging, consider the representative application of a millimeter-wave vehicular-mounted imaging system. Assume a center frequency of $f_0 = 75$ GHz and an available aperture length of 2 m. At this frequency, an element spacing of $d_0 = \lambda_0/2 = 2$ mm implies the need for 1000 array elements in order to fully populate the linear aperture. The simple line-of-sight point target model shown in Fig. 9 was used to simulate the array response over a frequency bandwidth of 1 GHz, which provides a 15 cm range resolution following pulse compression.

Modeling the transmitting source as a single isotropic antenna located at the center of the aperture, the frequency response was initially determined at the $N = 1000$ equally spaced receive element locations. The full standard array image is generated by first sorting the received data by range using the pulse-compression technique, and then applying (2) at each of the range bins.

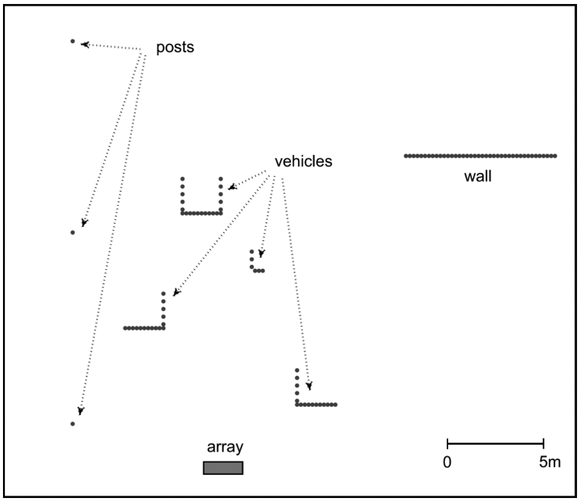

Fig. 9. Point source model.

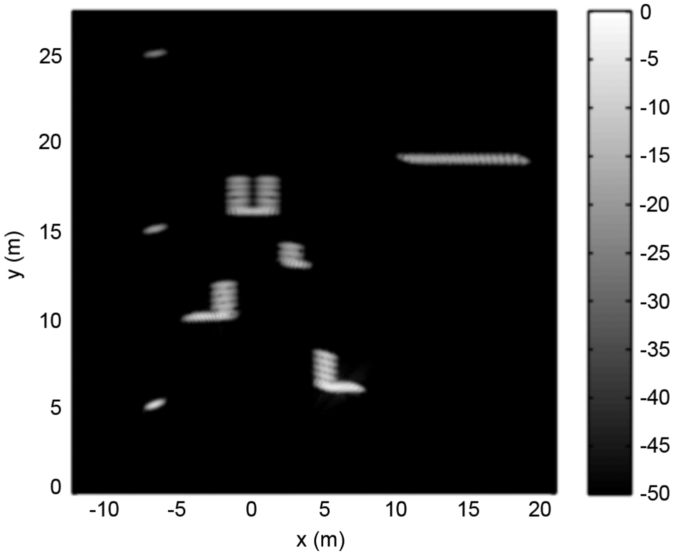

Fig. 10. Standard array image reconstruction, $N = 987$ elements with spacing $d_0 = \lambda_0/2$. SNR = 30 dB.

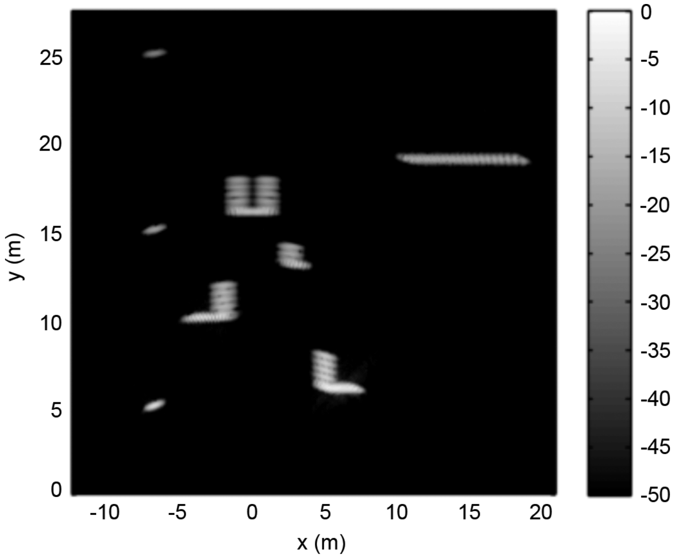

Fig. 11. Reconstructed image for the $(28, 47)$ multi-coset array with coset pattern $\mathcal{P} = \{0, 1, 2, 3, 4, 5, 10, 11, 12, 13, 15, 16, 19, 21, 22, 25, 26, 27, 30, 32, 34, 38, 39, 41, 42, 44, 45, 46\}$. SNR = 30 dB.

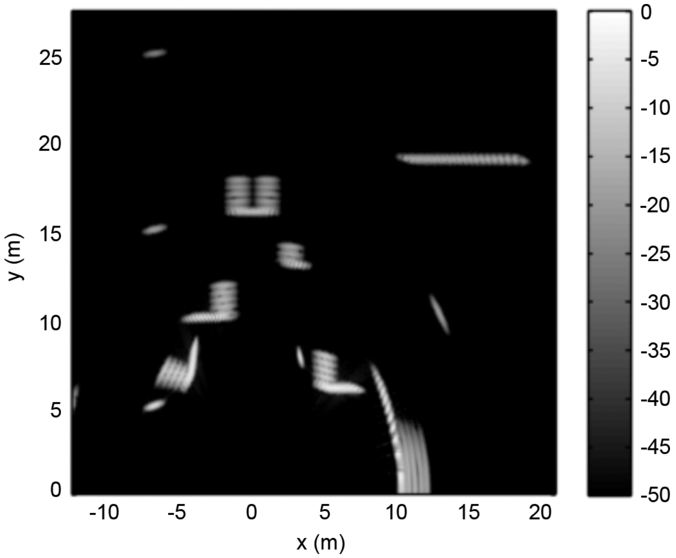

Fig. 12. Reconstructed image from the sparse uniform array of $N = 588$ elements with spacing $d = d_0/0.596 = 0.839\lambda$. SNR = 30 dB.

The image was partitioned into sectors of equal widths $\Delta\psi_L = 1/L$ for increasing values of L in order to observe maximum sector density $\rho_{s,L} = Q_{\max}/L$ over all ranges. Following a rapid decrease, $\rho_{s,L}$ begins to level off at about $L = 50$. Based on observations that prime values of L typically yield better conditioned measurement matrices, a coset period of $L = 47$ was selected. Adhering to the aperture constraint, this allows $M = 21$ coset periods for a total number of array elements $N = ML = 987$. Using all 987 elements to generate the standard array image with SNR = 30 dB yields the result shown in Fig. 10.

At $L = 47$ the maximum number of occupied sectors is $Q = 14$. A conservative choice for the number of cosets is $P = 2Q = 28$, resulting in an array with a density factor $\rho_A = 0.596$. Using the MCMC technique to design the coset pattern for the $(28, 47)$ multi-coset array with $N = 588$ elements, the resultant image is shown in Fig. 11. With this conservative choice of P, we see that the multi-coset array image reconstruction is nearly indistinguishable from the full array reconstruction.

For comparison, a uniform array with this same number of elements (corresponding to $d = d_0/0.596 = 0.839\lambda$) performs poorly, due to grating lobe effects, as shown in Fig. 12. Indeed, this array is unable to distinguish the direction of arrival for targets outside of $|\psi| < 0.30$ and copies of image targets appear in multiple locations.

The corresponding "bunched" coset pattern also performs poorly as shown in Fig. 13, as we would expect from our analysis. While the bunched pattern is able to determine the correct support at each range due to the conservative choice of P, it is evident that the poor conditioning of the associated

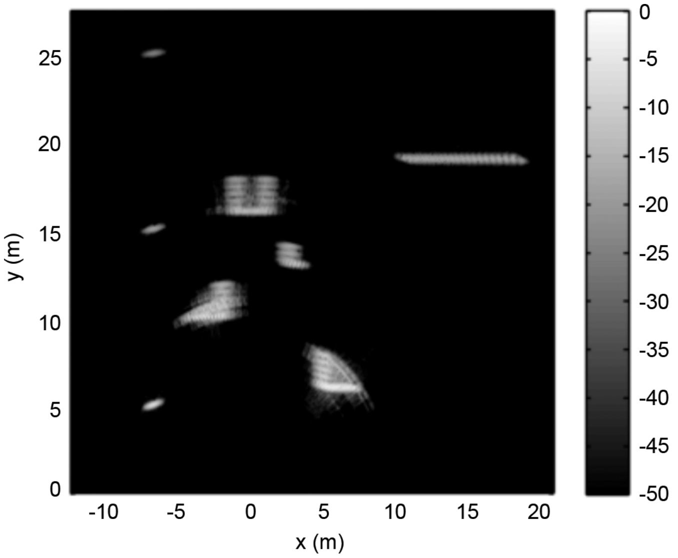

Fig. 13. Reconstructed image for the $(28, 47)$ multi-coset array with "bunched" coset pattern $\mathcal{P}_b = \{0, 1, \ldots, 27\}$. SNR = 30 dB.

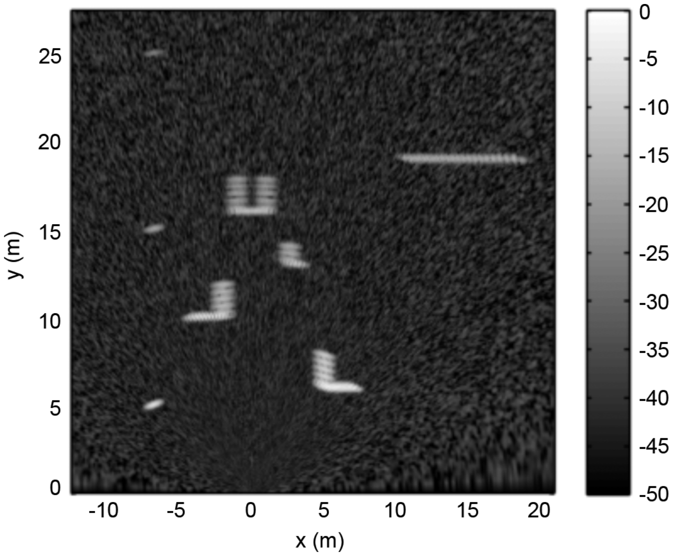

Fig. 14. Standard array image reconstruction, $N = 987$ elements with spacing $d_0 = \lambda_0/2$. SNR = 10 dB.

measurement matrix results in a significant magnification of the noise within this support.

The noise amplification characteristics associated with the bunched pattern are even more pronounced at low SNR. To illustrate this, Figs. 14, 15, and Fig. 16 show the image reconstructions at $\mathrm{SNR} = 10$ dB for the full 987 element array, the co-array designed multi-coset array, and the bunched multi-coset array, respectively.

Fig. 15 also emphasizes a significant feature of the multi-coset reconstruction. In contrast to the reconstruction from the full array in Fig. 14, in which the noise is distributed with relative uniformity throughout the image, the image in Fig. 15 has the noise eliminated in the sectors identified as inactive by the support recovery processing.

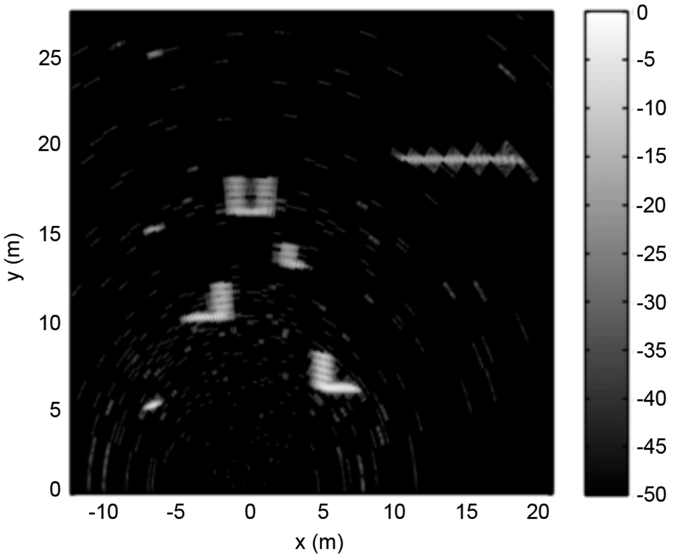

Fig. 15. Reconstructed image for the $(28, 47)$ multi-coset array with coset pattern $\mathcal{P}$ as in Fig. 11. SNR = 10 dB.

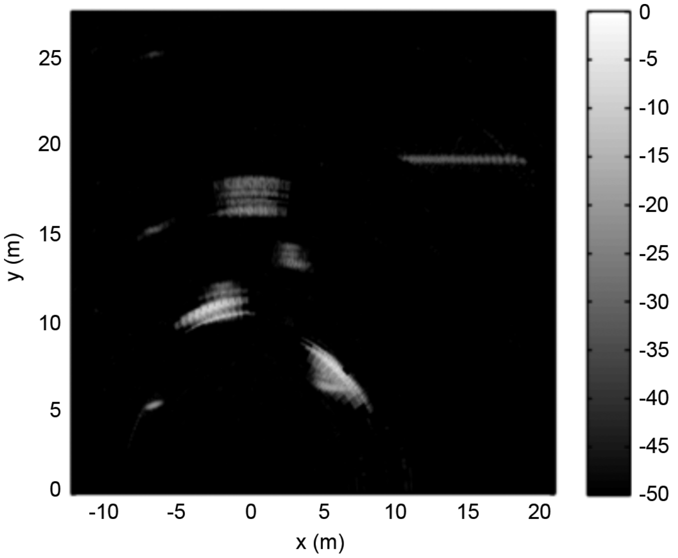

Fig. 16. Reconstructed image for the $(28, 47)$ multi-coset array with "bunched" coset pattern $\mathcal{P}_b = \{0, 1, \ldots, 27\}$. SNR = 10 dB.

C. Undersparse Arrays

Useful reconstructions can be obtained from multi-coset imaging even when the number of elements is strictly insufficient for the realized scene density, as we will now illustrate. In such cases, the associated reconstructions are most useful in conjunction with failure detection methods as developed in Section VI. In this 2-D imaging scenario, our BPE failure measure is applied at each range. Fig. 17 shows the reconstructed images for $P \leq Q = 14$. The bar immediately to the right of each reconstruction indicates the BPE at each range.

Due to the moderately aggressive choice of $P = 14$ for this scene, the image shown in Fig. 17(a) exhibits a mild degree of error at the ranges with the highest densities. This is to be expected as the number of cosets begins to be insufficient to accurately determine the supported sectors. In Fig. 17(b), the array

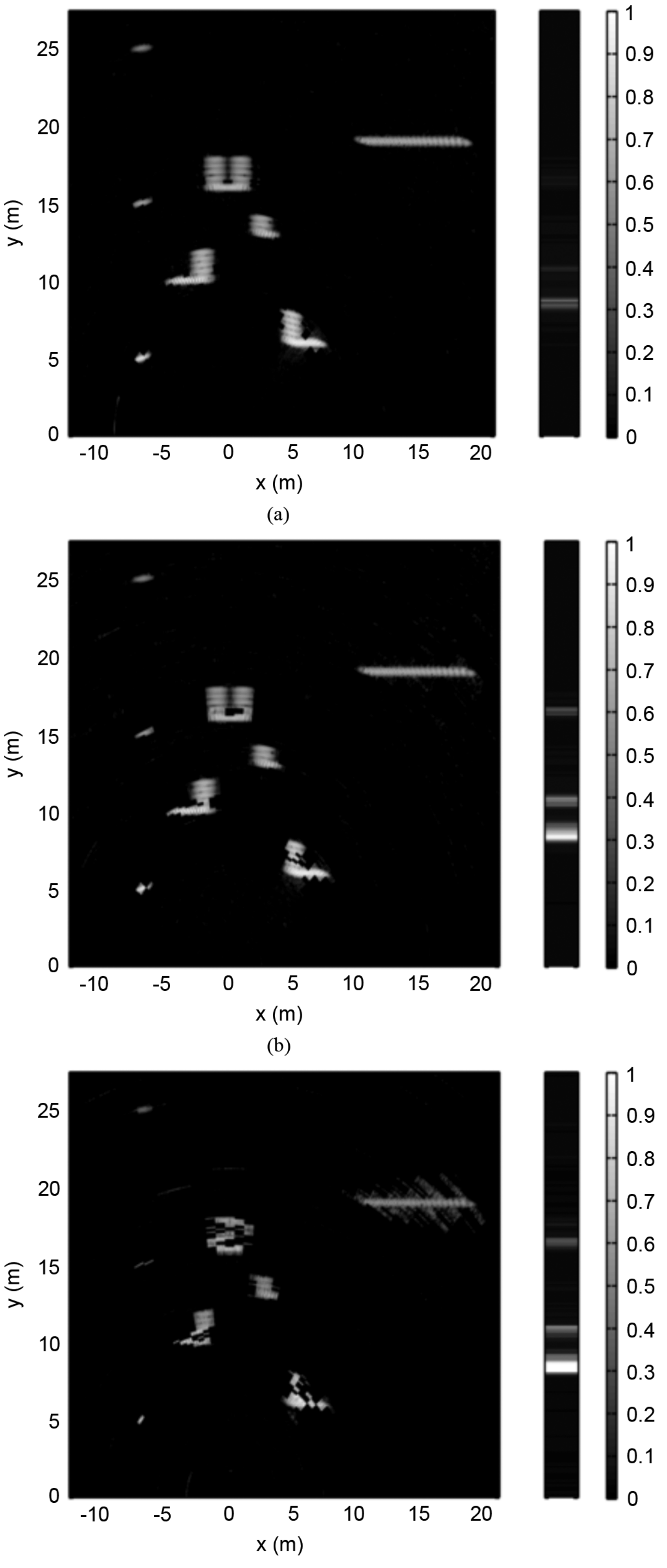

(a)

(b)

(c)

Fig. 17. Multi-coset images with failure detection, $L = 47$ and (a) $P = 14$, (b) $P = 9$, (c) $P = 5$. SNR = 30 dB.

has $P = 9$ cosets, and more severe errors begin to occur. A primary utility of having this range-dependent error indication is that when failures occur, the location can be identified and ignored, or judged with caution, without discarding results at other ranges that still have sufficiently low densities. In Fig. 17(c), the array retains $P = 5$ cosets, having reduced the total number of elements to 105 of the original $N = 987$. While the objects are showing noticeable levels of distortion, the gross features of the image are preserved—e.g., each target still being located by the support recovery algorithm—with the most egregious distortions being identified by the error indicator.

VIII. CONCLUDING REMARKS

This paper describes a novel framework based on multi-coset antennas for computationally efficient imaging from sparse arrays. The imaging architecture developed in this paper is potentially attractive for a range of emerging applications that would otherwise require significantly more antenna elements and/or processing chains than can be accommodated in practice.

Ultimately, there are many opportunities for further development suggested by this work. For example, much of our evaluation of the techniques has focused on scenes with uncorrelated sectors. In practice, multipath and other phenomena can give rise to correlations in the scene. And while we have mentioned techniques that can be used to enhance the performance of the system in such scenarios, a more detailed evaluation of such enhancements remains to be undertaken.

Additionally, the “soft” MUSIC algorithm developed in this work for support recovery would appear to have potential applications well beyond those considered in this paper. As such, it would be worth exploring how broadly applicable this version of MUSIC might be.

Similarly, our development leveraged valuable connections and perspectives from the problem of multi-coset sampling signals with sparse frequency support. As such, it would appear that the co-array design techniques developed in the present paper may directly or indirectly suggest efficient sampling patterns for use with spectrally sparse signals. This warrants further investigation.

It should also be re-emphasized that there is a growing interest in the use of multi-coset antenna architectures for other problems. Exploring the degree to which the techniques developed herein, and to what extent the techniques emerging in other contexts can be applied to the imaging setting of this paper, would also be worthwhile. Such an investigation is likely to reveal other valuable connections as well.

Finally, while our development has often emphasized imaging applications, in principle the techniques can be applied in a wide variety of radar and sonar environments requiring target detection and tracking. Ultimately, exploring such applications represents one of richest directions for further research on this topic.

REFERENCES

[1] Y. T. Lo and S. W. Lee, *Antenna Handbook: Antenna Theory*. New York, NY, USA: Van Nostrand Reinhold, 1993.

[2] R. J. Mailloux, *Phased Array Antenna Handbook*. Boston, MA, USA: Artech House, 2005.

[3] J. S. Herd, S. M. Duffy, and H. Steyskal, “Design considerations and results for an overlapped subarray radar antenna,” in *Proc. IEEE Aerospace Conf.*, 2005, pp. 1087–1092.

[4] R. O. Schmidt, “Multiple emitter location and signal parameter estimation,” *IEEE Trans. Antennas Propag.*, vol. 34, no. 3, pp. 276–280, Mar. 1986.

[5] Y. Kochman and G. W. Wornell, “Finite multi-coset sampling and sparse arrays,” in *Proc. Workshop on Inform. Theory and Applicat. (ITA)*, La Jolla, CA, USA, 2011, pp. 1–7.

[6] P. Pal and P. P. Vaidyanathan, “Nested arrays: A novel approach to array processing with enhanced degrees of freedom,” *IEEE Trans. Signal Process*, vol. 58, no. 8, pp. 4167–4181, 2010.

[7] P. P. Vaidyanathan and P. Pal, “Sparse sensing with co-prime samplers and arrays,” *IEEE Trans. Signal Process*, vol. 59, no. 2, pp. 573–586, 2011.

[8] P. Pal and P. P. Vaidyanathan, “Coprime sampling and the music algorithm,” in *Proc. IEEE Digital Signal Processing, Signal Processing Educ. Workshop (DSP/SPE)*, 2011, pp. 289–294.

[9] S. Shakeri, D. D. Ariananda, and G. Leus, “Direction of arrival estimation using sparse ruler array design,” in *Proc. IEEE Workshop on Signal Processing Advances in Wireless Commun. (SPAWC)*, 2012, pp. 525–529.

[10] M. E. Dominguez-Jimenez, N. Gonzalez-Prelcic, G. Vazquez-Vilar, and R. Lopez-Valcarce, “Design of universal multicoset sampling patterns for compressed sensing of multiband sparse signals,” in *Proc. IEEE Int. Conf. Acoust., Speech, Signal Process. (ICASSP)*, 2012, pp. 3337–3340.

[11] D. Romero and G. Leus, “Compressive covariance sampling,” in *Proc. Inform. Theory Applicat. Workshop (ITA)*, La Jolla, CA, USA, 2013, pp. 1–8.

[12] E. J. Candes and M. B. Wakin, “An introduction to compressive sampling,” *IEEE Signal Process. Mag.*, vol. 25, no. 2, pp. 21–30, 2008.

[13] D. Donoho, “Compressed sensing,” *IEEE Trans. Inf. Theory*, vol. 52, no. 4, pp. 1289–1306, 2006.

[14] P. Feng and Y. Bresler, “Spectrum-blind minimum-rate sampling and reconstruction of multiband signals,” in *Proc. IEEE Int. Conf. Acoust., Speech, Signal Process. (ICASSP)*, Atlanta, GA, USA, 1996, vol. 3, pp. 1688–1691.

[15] J. Chen and X. Huo, “Theoretical results on sparse representations of multiple-measurement vectors,” *IEEE Trans. Signal Process*, vol. 54, no. 12, pp. 4634–4643, 2006.

[16] M. Mishali and Y. C. Eldar, “Blind multiband signal reconstruction: Compressed sensing for analog signals,” *IEEE Trans. Signal Process*, vol. 57, no. 3, pp. 993–1009, 2009.

[17] S. Cotter, B. Rao, K. Engan, and K. Kreutz-Delgado, “Sparse solutions to linear inverse problems with multiple measurement vectors,” *IEEE Trans. Signal Process*, vol. 53, no. 7, pp. 2477–2488, 2005.

[18] K. Lee and Y. Bresler, “Subspace-augmented MUSIC for joint sparse recovery with any rank,” in *Proc. IEEE Workshop on Sensor Array, Multichannel Signal Process. (SAM)*, 2010, pp. 205–208.

[19] M. E. Davies and Y. C. Eldar, “Rank awareness in joint sparse recovery,” *IEEE Trans. Inf. Theory*, vol. 58, no. 2, pp. 1135–1146, 2012.

[20] J. M. Kim, O. K. Lee, and J.-C. Ye, “Compressive MUSIC: Revisiting the link between compressive sensing and array signal processing,” *IEEE Trans. Inf. Theory*, vol. 58, no. 1, pp. 278–301, 2012.

[21] R. A. Horn and C. R. Johnson, *Matrix analysis*. Cambridge, U.K.: Cambridge Univ. Press, 2012.

[22] J. A. Tropp, A. C. Gilbert, and M. J. Strauss, “Algorithms for simultaneous sparse approximation. Part I: greedy pursuit,” *Signal Processing*, vol. 86, no. 3, pp. 572–588, 2006.

[23] J. A. Tropp, “Algorithms for simultaneous sparse approximation. Part II: Convex relaxation,” *Signal Processing*, vol. 86, no. 3, pp. 589–602, 2006.

[24] D. Johnson and S. DeGraaf, “Improving the resolution of bearing in passive sonar arrays by eigenvalue analysis,” *IEEE Trans. Acoust., Speech, Signal Process*, vol. 30, no. 4, pp. 638–647, 1982.

[25] A. Moffet, “Minimum-redundancy linear arrays,” *IEEE Trans. Antennas Propag.*, vol. 16, no. 2, pp. 172–175, 1968.

[26] S. Kirkpatrick, C. D. Gelatt, and M. P. Vecchi, “Optimization by simulated annealing,” *Sci.*, vol. 220, pp. 671–680, 1983.

James D. Krieger received the B.S. degree in physics from the University of California at Santa Barbara, CA, USA, in 2000 and the M.S. degree in electrical engineering from the Ohio State University, Columbus, OH, USA, in 2005. He is currently pursuing the Ph.D degree in electrical engineering and computer science from the Massachusetts Institute of Technology, Cambridge, MA, USA.

From 2001 to 2003 and 2005 to 2008, he was a Researcher at MIT Lincoln Laboratory, Lexington, where his primary focus was the development and analysis of wideband antenna and array systems.

Yuval Kochman received the B.Sc. (*cum laude*), M.Sc. (*cum laude*) and Ph.D. degrees from Tel Aviv University, Tel Aviv, Israel, in 1993, 2003 and 2010, respectively, all in electrical engineering.

During 2009–2011, he was a Postdoctoral Associate at the Signals, Information and Algorithms Laboratory at the Massachusetts Institute of Technology (MIT), Cambridge, MA, USA. Since 2012, he has been with the School of Computer Science and Engineering at the Hebrew University of Jerusalem. Outside academia, he has worked in the areas of radar and digital communications. His research interests include information theory, communications and signal processing.

Gregory W. Wornell (S’83–M’91–SM’00–F’04) received the B.A.Sc. degree in electrical engineering from the University of British Columbia, Vancouver, BC, Canada, and the S.M. and Ph.D. degrees in electrical engineering and computer science from the Massachusetts Institute of Technology (MIT), Cambridge, MA, USA, in 1985, 1987, and 1991, respectively.

Since 1991, he has been on the faculty at MIT, where he is the Sumitomo Professor of Engineering in the department of Electrical Engineering and Computer Science (EECS). He leads the Signals, Information, and Algorithms Laboratory in the Research Laboratory of Electronics, and co-chairs the EECS department graduate program. He has held visiting appointments at the former AT&T Bell Laboratories, Murray Hill, NJ, USA, the University of California, Berkeley, CA, USA, and Hewlett-Packard Laboratories, Palo Alto, CA, USA. His research interests and publications span the areas of signal processing, digital communication, and information theory, and include algorithms and architectures for wireless networks, sensing and imaging systems, digitally-enhanced analog circuits and systems, multimedia applications, and aspects of computational biology and neuroscience.

Dr. Wornell has been involved in the Information Theory and Signal Processing Societies of the IEEE in a variety of capacities, and maintains a number of close industrial relationships and activities. He has won a number of awards for both his research and teaching.